Measurements of the parameter dependencies of the bootstrap current in the W7-X stellarator

U. Neuner[1], K. Rahbarnia[1], C.D. Beidler[1], A. Dinklage[1], Y. Turkin[1], T. Stange[1], T. Andreeva[1], J. Schilling[1], H. Thomsen[1], M. Beurskens[1], S. Bozhenkov[1], K.J. Brunner[1], H. Damm[1], G. Fuchert[1], J. Geiger[1], U. Hergenhahn[1], U. Höfel[1], J. Knauer[1], M. Krychowiak[1], S. Kwak[1], A. Langenberg[1], N. Pablant[2], E. Pasch[1], A. Pavone[1], E.R. Scott[1,3], J. Svensson[1], H. Trimino Mora[1] and the Wendelstein 7-X team

[1] *Max-Planck-Institut für Plasmaphysik, Greifswald, Germany*

[2] *Princeton Plasma Physics Laboratory, Princeton, United States*

[3] *Department of Engineering Physics, University of Wisconsin–Madison, Madison, United States*

Abstract

Intrinsic, diffusion-driven toroidal (bootstrap) currents between -7 and 17 kA were measured in the optimised stellarator Wendelstein 7-X for several magnetic configurations at line-integrated plasma densities between 2×10^{19} and 1.6×10^{20} m^{-2} and heating powers between 0.5 and 6 MW. The sign of the bootstrap current changes with field reversal, and its magnitude decreases with the mirror term and the rotational transform of the magnetic configuration, as well as the line-integrated plasma density and increases with the heating power. Both the absolute values and the dependencies agree with neoclassical calculations within their respective uncertainties, confirming the neoclassical optimisation of W7-X for small bootstrap currents.

1. Introduction

1.1 Wendelstein 7-X

Wendelstein 7-X (W7-X) [Nührenberg 1986, Klinger 2013, Klinger 2019] is an optimised stellarator. In the recent operational phase OP1.2b, boronisation facilitated a rise in the maximum controllable plasma density and the maximum pulse length, and operation in pure hydrogen became possible [Sereda 2020]. W7-X has so far reached a maximum pulse length of 100 s and a maximum plasma energy of 1.1 MJ. The heating method employed for the experimental programs reported in this work is electron cyclotron resonance heating (ECRH). OP1.2b was also characterised by a marked increase in the quality of the profile data of the plasma parameters by improvements in various diagnostics and data analysis tools. This, in turn, facilitated a higher precision of the theoretical simulations of the plasma.

The magnetic configurations of W7-X allow for a variation of, among others, the rotational transform and the mirror term (the average variation of the magnetic field strength along the plasma column). These configurations resulted from an optimisation aiming for several goals, one of which concerned the bootstrap current.

1.2 Bootstrap current

The bootstrap current is a net toroidal current (in the literature the term is also used for the underlying parallel current density) [Hogan 1981] in a magnetically confined toroidal plasma driven by the temperature and density gradients [Bickerton 1971, Galeev 1971, Catto 2020]. Solutions of the linearized drift kinetic equation always exhibit a net parallel current flow within the flux surfaces of toroidal confinement devices, as soon as the radial gradients of density, temperature or electrostatic potential are non-zero on the flux surface. This bootstrap current is a neoclassical effect that arises because individual particle trajectories are not confined to a single flux surface. It can attain large values at reactor-relevant collisionalities where the influence of trapped-particle orbits becomes most pronounced. In tokamaks, the bootstrap current generally flows in the same direction as the net plasma current, while in stellarators the flow can be directed in both directions.

Bootstrap current densities alter the radial profile of the rotational transform (ι). Should ι cross a low-order rational value, island chains may occur, degrading the confinement. A non-vanishing total current alters the edge ι. This, in turn, affects the position of the X-points that channel outward-flowing plasma to divertor regions where recycling and exhaust are to take place.

Whereas early work [Maaßberg 1993] expected the effect of the bootstrap current on the profile of the rotational transform is to be negligible for W7-X, more recent work [Maaßberg 2009] showed ι to cross the 1/1 rational surface deep inside the plasma. The effect of the bootstrap current on the edge ι of W7-X will affect the external islands, shifting the strike line positions on the targets and generally changing the deposition patterns, possibly overloading parts of the divertor [Geiger 2010, Lore 2014, Lumsdaine 2016].

Suppression of the bootstrap current is not an inherent property of all stellarators [Boozer 1989]. It requires an appropriate choice of magnetic field geometry, as was undertaken in the optimisation of W7-X [Nührenberg 1986, Beidler 1990, Grieger 1992 Phys. Fluids B, Grieger 1992 Fusion Technol.]. However, the cancellation of the bootstrap current contributions attributable to the toroidal and helical components of the magnetic field is only achieved for certain magnetic configurations and plasma parameters of W7-X. In contrast, had the device been perfectly quasi-isodynamic, i.e. if the neoclassical optimisation had been done so well that all collisionless orbits were confined, then the bootstrap current would vanish [Helander 2009 and 2011].

This, then, motivated the work presented in this paper. The goal was to provide values of the measured bootstrap current to assess where it is sufficiently small, and where countermeasures are needed (and how large these need to be). In addition, to verify for a large parameter space the applicability of the neoclassical theory in the optimisation of W7-X for small bootstrap currents.

1.3 Status of research on bootstrap currents in stellarators

Various stellarators report on measuring or neoclassically calculating their bootstrap current, also benchmarking between codes. W.L.OCTUPOLE [Zarnstorff 1984], Proto-Cleo [Treffert 1984], Heliotron-E [Besshou 1984], Uragan-3 [Gutarev 1987], Wendelstein 7-A [Gasparino 1988], LHD [Okamoto 1990, Huang 2017], ATF [Murakami 1991], Wendelstein 7-AS [Erckmann 1992], CHS [Isobe 2002], Heliotron-J [Nagasaki 2006], HSX [Schmitt 2007], Uragan-3M [Pashnev 2008], TJ-II [Velasco

2011, Camacho 2017]. Measurements and neoclassical calculations generally showed good agreement, with only one of the above [Isobe 2002] as an exception.

In the first operational phase of W7-X, OP1.1, with the machine being operated in a limiter configuration [Klinger 2017, Wolf 2017], a correlation of a decrease of the toroidal current with an increase of the mirror term as expected from neoclassical theory was observed [Sunn Pedersen 2017]. Furthermore, extrapolations of the observed toroidal currents were found to be in agreement with neoclassical calculations of their steady state values. The ratio of the latter for the two magnetic configurations showed good agreement with the ratio of the measured toroidal currents at the end of the discharge [Dinklage 2018]. In the following operational phase OP1.2a, prior to which an uncooled test divertor was installed instead of the limiter, values for the bootstrap current were obtained via an exponential fit to the measured toroidal current. The variation of the mirror term was expanded, showing again the previous correlation. Additionally, a correlation of a decrease of the toroidal current with an increase of the rotational transform could be demonstrated, this too being expected from neoclassical theory [Andreeva 2019]. Early during the last operational phase OP1.2b, the variation of the rotational transform was expanded, showing the same correlation as previously. Here, the reported toroidal currents could be reproduced in neoclassical calculations with the NTSS code [Turkin 2006, Turkin 2011] under the assumption of a small electron cyclotron driven current [Klinger 2019].

These initial measurements of the toroidal current of W7-X confirmed the applicability of neoclassical theory in the optimisation of W7-X for a small bootstrap current. They moreover verified that this optimisation goal was achieved. The parameter range covered, however, was rather limited and there was never a direct comparison of measured and calculated bootstrap currents. The work presented in this paper not only vastly increases the number of data points, but also more than doubles the number of parameters varied. The latter allows, for the first time, to separate the effects of the different parameters on the bootstrap current.

2. Method: From Rogowski coil signal to bootstrap current

2.1 Calibration

One of the Rogowski coils [Endler 2015, Rahbarnia 2016] mounted inside the plasma vessel of W7-X was employed to measure the net toroidal current, several others mounted either on the inside or on the outside of the plasma vessel for comparison. The voltage signal from the Rogowski coil is digitised [Werner 2006], numerically integrated and scaled to yield the current through the coil. The integration is carried out similar to the procedure that is applied to the diamagnetic loop raw signals, as described in [Rahbarnia 2018].

The sensitivity factor employed in the scaling process can be calculated from the size and winding density of the coil, but the precision is increased by an order of magnitude by the calibration. Moreover, the calibration takes into account all spurious effects of the electronics involved in the data collection and processing. The calibration took place by installing a toroidal metal conductor close to the magnetic axis, and using a current clamp to measure a current applied to this conductor [Neuner 2017]. The Rogowski coils should in this way have been calibrated to within the uncertainty of the current clamp of 3 %, with even smaller relative deviations between different coils.

A comparison of the currents derived from several Rogowski coils located at different toroidal positions, however, showed deviations up to 4 % (figure 1). These might be caused by small poloidal gaps and non-uniformities in the winding density that make the coils susceptible not only to the total current through the loop spanned by the coil, but also to the current density distribution in the vicinity of the coil. The latter differs because the coil positions differ. Temperature differences or electronic drifts are possible other causes.

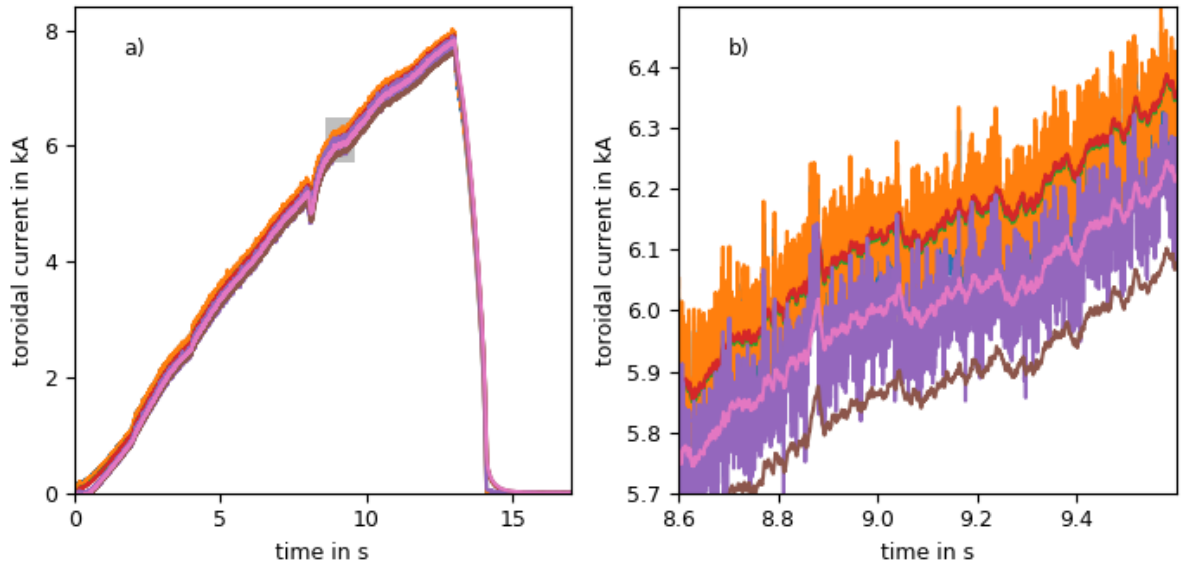

Figure 1. Comparison of the total toroidal current measured with several Rogowski coils mounted on the inner and outer surface of the plasma vessel wall during an exemplary program (a) and zoom-in on the area underlaid in grey (b).

Since dampening of the outer coils by induced currents in the plasma vessel may also contribute to differences between coils, in addition to the calibration with the direct current, an alternating current at frequencies between 6 and 1000 Hz was also employed. Over the whole frequency range currents in conducting components are induced, significantly increasing or decreasing the outputs of individual Rogowski coil segments. Whereas an ideal Rogowski coil will measure only the total current through the surface spanned by the coil, the small gaps and non-uniformities in our coils lead to a small scatter between different coils, including unrealistic values above 1 (figure 2).

For the inner coils, it was found that the measurement is significantly dampened only above 100 Hz. The dampening onset might not be governed by currents induced in the first wall or the divertor but rather by currents induced in supports and walkways installed only during the calibration so that the dampening onset during the operational phases might be above 100 Hz. The outer coils were significantly dampened over the whole observed frequency range. No measurements below 6 Hz were performed, but when the DC calibration current was switched on, the Rogowski coils mounted on the outside of the plasma vessel reached their steady state values after one second. For the signal range below 1 Hz used in this work, dampening can therefore be neglected even for the outer coils.

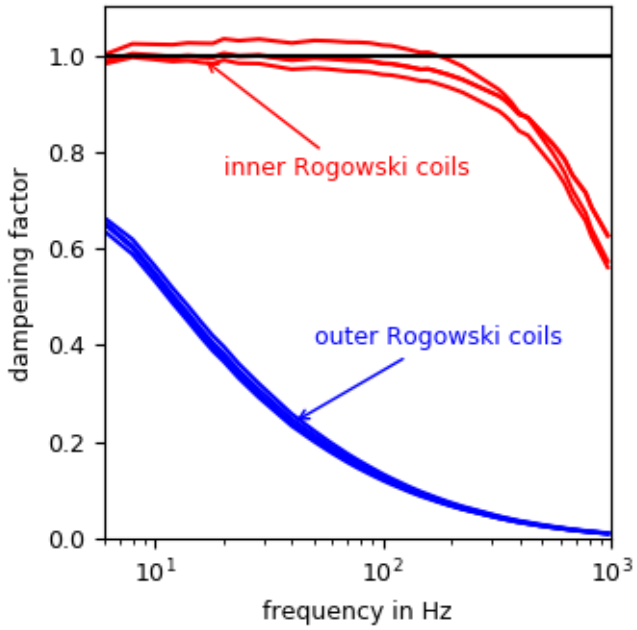

Figure 2. Dampening of the Rogowski coil signals as a function of the frequency for Rogowski coils mounted on the inside of the plasma vessel (red) and Rogowski coils mounted on the outside of the plasma vessel (blue). The scatter between the curves gives an indication of the error.

2.2 Currents outside the last closed flux surface

A Rogowski coil measures the current through the surface spanned by the coil. In the case of the inner Rogowski coils in W7-X this potentially comprises currents in the shielding pipes of the Rogowski coils, the low pressure gas environment between plasma vessel and first wall where the coils are situated, the components in the plasma vessel (first wall and divertor), the private flux region, the external islands, and core plasma currents inside the last closed flux surface (separatrix) (figure 3).

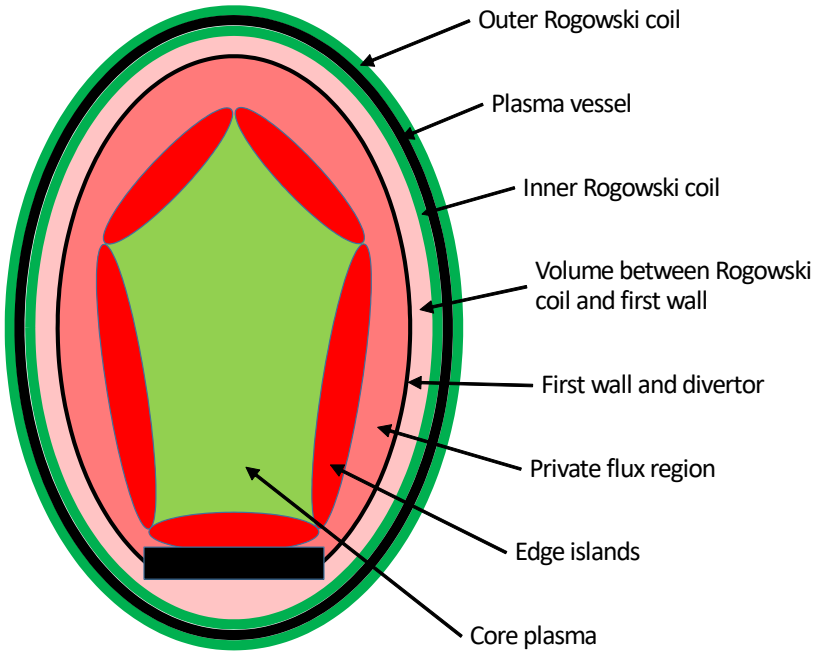

Figure 3. Simplified schematics of a poloidal cross section showing the areas where current measured by the Rogowski coil could be situated.

Before inferring core plasma currents from inner Rogowski coil signals, all other potential currents that would give rise to a signal in the Rogowski coil have to be discussed. Causes for such currents outside the last closed flux surface could be electric fields, diffusion or drifts. Driving voltages could have their origin in induction (e.g. from fast changing plasma currents), static charges on insulators or stray radiation from the ECRH scheme. In all electrically conductive regions adjacent to current carrying regions, current diffusion can lead to currents. Current in the external islands and further outside could originate from parallel gradients drifts [Hammond 2019] or thermo-diffusion [Rack 2012].

Induced currents in the shielding pipes, which encase the Rogowski coils to protect them from ECRH stray radiation, are quickly dampened by the resistance of the copper material (dampening onset above 1000 Hz [Endler 2015]) so as not to affect the slow signals (< 1 Hz) investigated in this work.

Because the plasma vessel is filled with low-pressure gas, discharges along magnetic field lines are conceivable between components. Arc footprints in the space between plasma vessel wall and first wall have been observed [Dhard 2020]. Such discharges could lead to currents through the Rogowski coil. The fact that the coils outside the plasma vessel show the same magnitude of current as those within (figure 1) rule out local, i.e. not fully toroidal current loops within the uncertainty of the calibration, since those would interlock with the inner Rogowski coils only, but not with the outer ones.

Fast changes of the toroidal plasma current or any other current will lead to a loop voltage in the first wall and the divertor, and potentially, depending on the segmentation and fixation (and thereby electrical connection) of these components, to currents affecting the output of the Rogowski coil. As experienced during the calibration, Ohmic damping makes this a high-frequency phenomenon (> 100 Hz or larger), thus not affecting the work presented here (< 1 Hz).

Neoclassical calculations of the radial current density distribution with the NTSS code show vanishing edge current density, thereby ruling out current diffusion across the separatrix into the islands and beyond for stable plasma conditions.

E × B and curvature drift effects and parallel density gradients may cause currents along magnetic field lines connecting different divertors. Taking the measured value of 100 mA / mm² as reported by [Hammond 2019] for the current density and multiplying it by a cross sectional area of 1000 mm² of a current tube whose footprint is the strike line, one arrives at a total current of 0.1 kA. Since the current density was only a local measurement, it is however not known if the individual current tubes add up to form a net total toroidal current or if their toroidal components rather cancel each other out. The current densities reported did change in magnitude with the plasma density, but a comprehensive study of their dependence on the plasma parameters is still not yet available. Asymmetries, e.g. in the magnetic field or the divertor positions, may cause otherwise symmetric currents to form a net toroidal current.

In summary, although it is justified to neglect many currents that might be flowing outside the last closed flux surface, there are some for which no upper limit could be found. As was done in the previous works mentioned in section 1.3, we are forced to adopt a heuristic approach to neglect all currents outside the last closed flux surface in this paper and attribute the current measured by the Rogowski coil to the toroidal current of the core plasma. At the beginning of the discussion in section

4.1 the necessary check if this is a valid thing to do will be performed using the obtained results in chapter 3. The error introduced by this heuristic method is, given the instrumentation of W-X, not quantifiable.

2.3 Accounting for the shielding current

The core plasma current, i.e. the total current inside the last closed flux surface, includes an induced shielding current that is counteracting any change to the current in the core plasma. Since the conductance of the plasma in which this current is flowing is finite, the shielding current is resistively dampened. This can be exploited to separate it from the other current components.

To do so, the plasma parameters (with the exception of the shielding current) need to be constant over a time in the order of the decay time of the shielding current. Even the profile shape of the shielding current density needs to be stationary. The latter was checked by making sure that the time before this interval was always long enough for the radial diffusion of the shielding current to have largely taken place (several skin times).

The measured time trace of the total current, the best substitute available for the core plasma current, is then fitted by a function describing a constant current from which an exponentially decaying shielding current is subtracted (see e.g. figs 4, 7, 8 and 9):

$$I_{\mathrm{CP}}(t) = I_{\mathrm{as}} - I_{\mathrm{S}}\mathrm{e}^{-(t-t_{\mathrm{s}})/\tau}.$$

where I_{CP} is the core plasma current, I_{as} the asymptotic value of the core plasma current, t the time, t_s the time of the start of the fit interval, I_S the shielding current at $t = t_s$, and τ the decay time of the shielding current. No assumptions on I_S and τ were made, together with I_{as} they were free parameters in the fit.

[Andreeva 2019] and [Neuner 2019] include results obtained with this method, but the method itself is first described here. It expands on the projection of steady state values used by [Schmitt 2007] in that it includes arbitrary plasma histories, e.g. plasma start-up phases. This is necessary because at W7-X achieving stable density typically takes a significant part of the total program length, and more generally because of the segmented program approach where a to-be-used time window can be preceded by many uncorrelated plasma phases. Alternative methods are the use of a transformer to achieve close to zero toroidal current [Erckmann 1992] (which W7-X does not have) or to only use plasma pulses at least several times as long as the decay time of the shielding current (only very rarely achieved in W7-X so far). The time necessary for the latter might be reduced with ECCD, but this is difficult to achieve and even more difficult to assess.

The fit formula was checked against data from an experimental program where the total current comes extremely close to its asymptotic value (figure 4). A fit to a time window typically available for most programs yields the asymptotic value gained with a fit to the whole available time window to within less than 5 %. This check was necessary because the shielding current is spread over the plasma radius, and the plasma temperature and density, and hence the plasma resistivity, vary over the radius. The fitting method approximates this with a single resistivity, thereby assuming the current is limited to a small radial range. The comparison with a long experimental program validated the assumption.

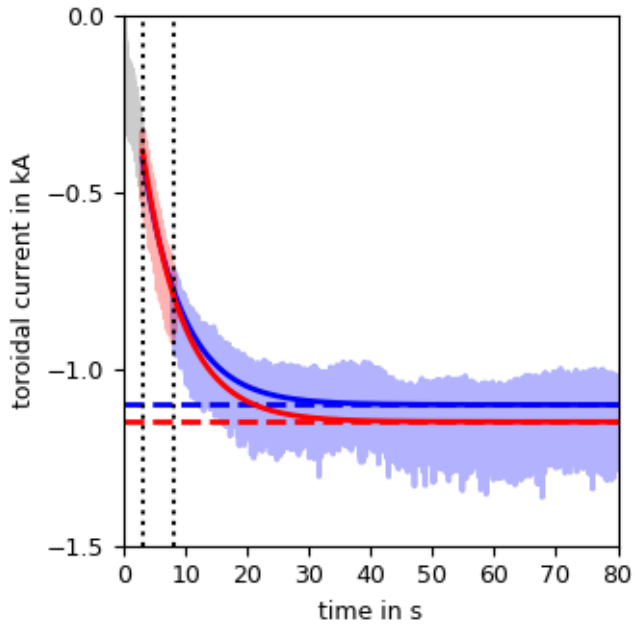

Figure 4. Validation of fitting the shielding current with a single exponential curve. The fit (red) to the time interval 3 – 8 s (light red) yields an asymptotic value of -1150 A (red dashed), a fit (blue) to the full available interval of 3 – 80 s (light red and light blue) yields -1102 A (blue dashed). Plasma parameters were constant between 3 and 80 s. The decay time of the shielding current is 6.5 s.

A variation of the plasma density and temperature during the fit interval (a few percent were allowed to include a data set into this work) will lead to a variation of the bootstrap current and thus the asymptotic current within the fit interval. The shielding current will follow the varying asymptotic current, while at the same time being exponentially dampened. The sensitivity of the fit result for the asymptotic value to this variation is as follows: In the case of noisy or decreasing absolute values of the asymptotic current, the fit delivers an average value. In the case of increasing absolute values of the asymptotic current, the fit gives an upper limit only, while the last measured current gives a lower limit, and the difference between the two needs to be treated as an error.

Combining all these considerations, the uncertainty in the inferred shielding currents were found to be smaller than ±1 kA for the programs reported in this work.

2.4 Current drive

The ECRH provides both heating and electron cyclotron current drive (ECCD). After subtraction of the shielding current from the measured current (practically, this was done by simply using the asymptotic value that was one of the outputs of the fit procedure), the resulting current in the plasma core is the sum of the bootstrap current and the ECCD. These two cannot be experimentally differentiated. The ECRH was therefore set so as to nominally produce no current drive (perpendicular injection).

The contribution to the experimental error from unintentional current drive by the ECRH (the horizontal angle of injection can be prescribed only to a finite precision of approximately ±0.5 °) is expected to be some 100 A in most cases and somewhat more at low densities, the driven current being calculated via ray tracing [Marushchenko 2014, Kapper 2016].

2.5 Overall uncertainty

The best guess for the overall uncertainty in the measured bootstrap currents is for it to be, taking all considerations discussed in the "Method" section into account, in the range of ±2 kA.

3. Results: Bootstrap currents

3.1 Parameter range

When planning the bootstrap current measurements, the goal was to gain the most confidence in neoclassical theory being applied to the bootstrap current of W7-X with a limited number of experimental programs. To achieve this, the governing idea was to use just two programs to vary any parameter, but to vary as many parameters as possible. Experimental programs had therefore been proposed for campaign OP1.2b to measure the dependence of the bootstrap current on the rotational transform, the mirror term, the inward / outward shift and the field direction of the magnetic configuration, the plasma density, the heating power and the gas species. Due to scarcity of experimental time, only the programs measuring the power and density dependency of the bootstrap current in the high-mirror configuration in hydrogen were performed. To augment the results of these dedicated programs, a data mining approach was employed. All programs of operational phase OP1.2b without intentional current drive were scanned for time windows of sufficiently constant plasma parameters that were long enough to perform the fit procedure necessary for evaluating the shielding current. This yielded a total of 134 intervals in which a bootstrap current could be inferred.

All results were obtained in hydrogen plasmas, the principal working gas of OP1.2b. The most data (68 values) were obtained in the standard magnetic configuration, a reflection of the fact that most programs were performed in this configuration. Of the mirror term variation, only the high-mirror configuration was realised, yielding four values. The variation of the rotational transform is reflected in the high-ι, intermediate-ι (a limiter configuration with ι between standard and high-ι) and low-ι configurations with 20, 4 and 7 values respectively. In the low-ι configuration, the field reversal was realised, yielding 31 values. For a definition of the magnetic configurations, see refs. [Andreeva 2002, Geiger 2015].

ECRH heating powers range from 0.5 MW (employing one gyrotron) to 6 MW (employing nine gyrotrons), corresponding to the capabilities of W7-X during OP1.2b. Line-integrated densities range from 2×10^{19} m^{-2} to 1.6×10^{20} m^{-2}, with the high densities being achievable at high heating powers only, since the correspondingly large radiation losses have to be overcome by sufficient heating.

Measurements from a suite of diagnostics [Krychowiak 2016] are analysed and combined in the Bayesian Minerva framework [Svensson 2007] to yield temperature and density profiles. Electron temperature and density profiles are measured by Thomson scattering [Pasch 2016]. Electron density profiles are validated by line-integrated interferometry measurements [Knauer 2016]. Ion temperature profiles are determined by an x-ray imaging spectrometer [Pablant 2016, Langenberg 2019]. Ion densities are estimated with a dilution factor obtained from mean values of the effective

charge state Z_{eff} [Pavone 2019, Pavone 2020] assuming fully ionised carbon as the main impurity. The profile data are mapped on magnetic flux surfaces using appropriately chosen equilibrium calculations with the VMEC code [Hirshman 1986, Grahl 2017, Andreeva 2019]. The data are fitted with smooth curves resulting from Gaussian process regression [Chilenski 2015] also delivering estimates for fitting errors as indicated by the shaded areas in figure 5.

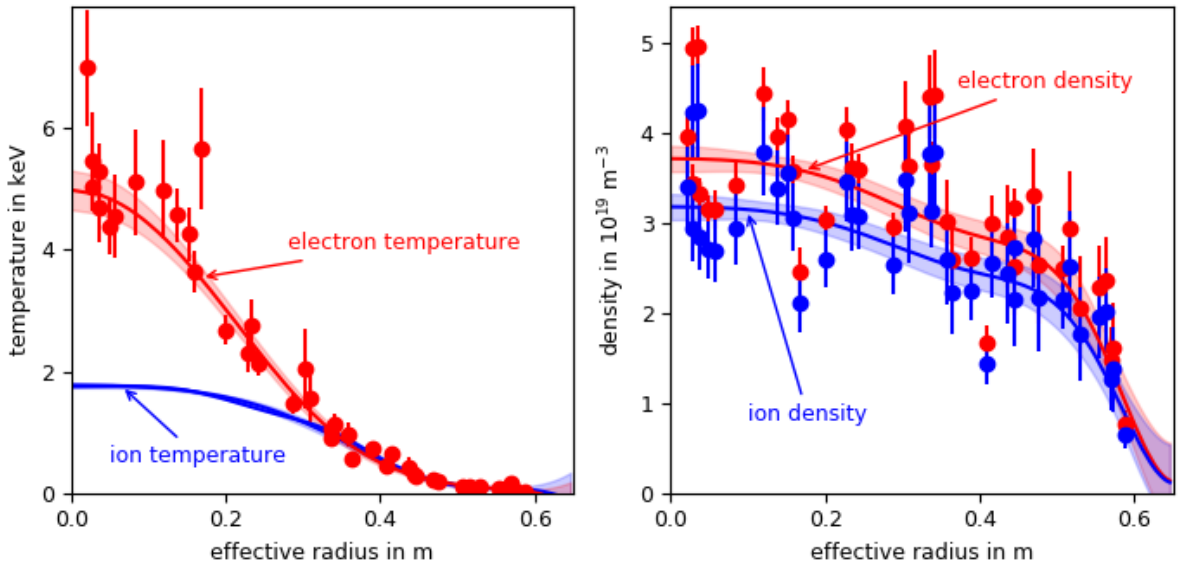

Figure 5. Exemplary temperature and density profiles.

For low densities and on-axis ECR heating, the temperature profiles are peaked with central electron temperatures significantly larger than central ion temperatures. These conditions typically lead to core electron-root confinement [Yokoyama 2007, Pablant 2018] with strong positive radial electric fields in the plasma core. With increasing densities, the electron and ion temperatures tend to equilibrate and the radial electric field becomes negative throughout the plasma volume. Density profiles are flat or slightly peaked for gas-fuelled programs (figure 5).

The bootstrap currents obtained in the way described in the "Methods" section varied between -7 and 5 kA for the high-mirror and high-ι configurations, which are optimised for small bootstrap currents, and between -3 and 17 kA for the standard, intermediate (limiter) and low-ι configurations. The sign convention of toroidal currents at W7-X is thus that (if the magnetic field is not reversed) positive currents flow clockwise as seen from above, opposite to the direction of the main toroidal magnetic field, increase the rotational transform and shift the edge islands inward.

Zero bootstrap current was achieved – within the uncertainties – in all magnetic configurations at a configuration and heating-power-specific line-integrated density between 2×10^{19} m^{-2} and approximately 1×10^{20} m^{-2}.

For some of the experimental programs, neoclassical simulations with the NTSS code (based on the DKES code) were performed. These were based on the fitted profiles derived from the measurements of the plasma parameters as described above. The uncertainties in the fitted profiles translated into uncertainties in the calculated bootstrap currents. The radial electric field was obtained by solving the ambipolarity constraint [Turkin 2011]. The ten programs chosen represent the maximal variation in mirror term, rotational transform, heating power, plasma density, and, consequently, bootstrap current. Since the profile evaluation is an elaborate process, no additional programs were looked into.

The calculations tend to underestimate the measurements, but, given the uncertainties, the difference is not statistically significant (figure 6). The non-random, systematic part of the uncertainties might account for the fact that all but one of the measured values are larger than their calculated counterparts.

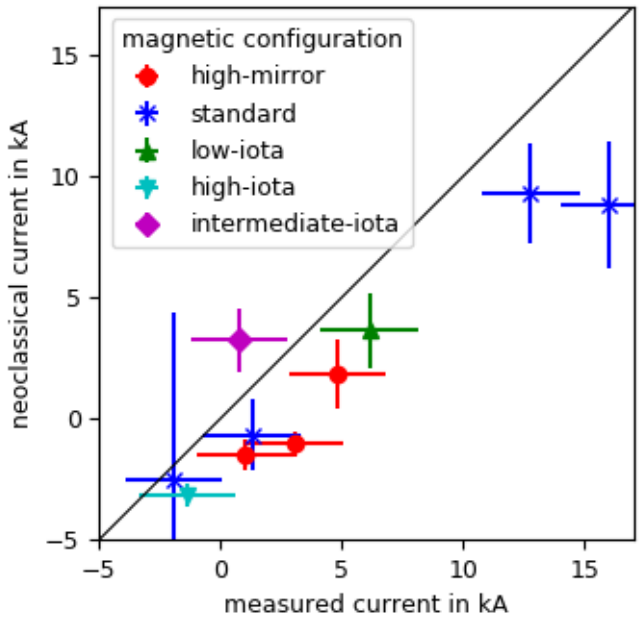

Figure 6. Comparison of the neoclassically calculated bootstrap currents to the measured bootstrap currents.

3.2 Dependence of the bootstrap current on the experimental parameters

3.2.1 Dependence on the magnetic configuration

For the dependence of the bootstrap current on the mirror term, the rotational transform and the field direction one example each is shown. In all cases, at other densities and heating powers the effect is either smaller than shown, too small to be distinguishable from the uncertainties or no experimental data is available.

Increasing the mirror term in the magnetic configuration from the standard configuration to the high-mirror configuration while keeping the heating power and the line-integrated density constant at 1 MW and 2×10^{19} m^{-2}, respectively, decreases the bootstrap current from 4.5 to 0.3 kA (figure 7).

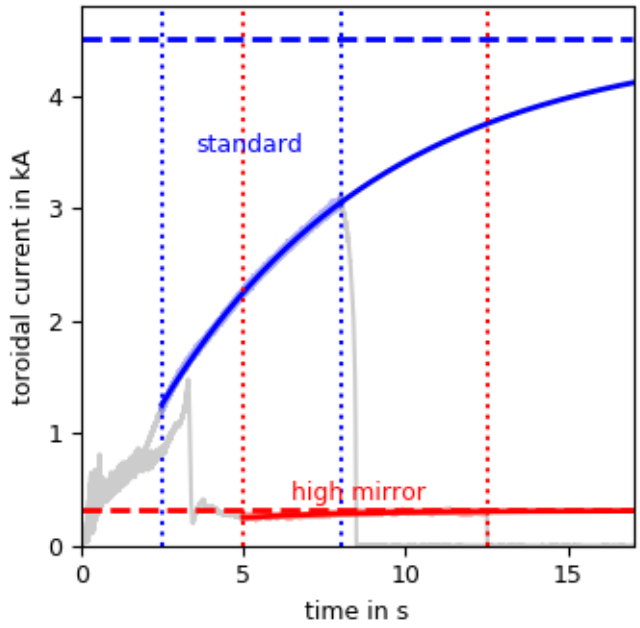

Figure 7. Dependence of the bootstrap current on the mirror term: standard (blue) and high-mirror (red) magnetic configurations. Time traces and fit (solid lines), fitting window (dotted lines) and asymptotic value (dashed lines).

The rotational transform was increased from the low-ɩ (edge ɩ equal to 5 / 6) via the standard-ɩ (edge ɩ equal to 1) to the high-ɩ (edge ɩ equal to 5 / 4) magnetic configuration. While doing so, the heating power and the line-integrated density were kept constant at 2 MW and 5×10^{19} m^{-2}, respectively. This increase in the rotational transform is associated with a decrease in the bootstrap current from 4.5 via 2.5 to 1.0 kA (figure 8).

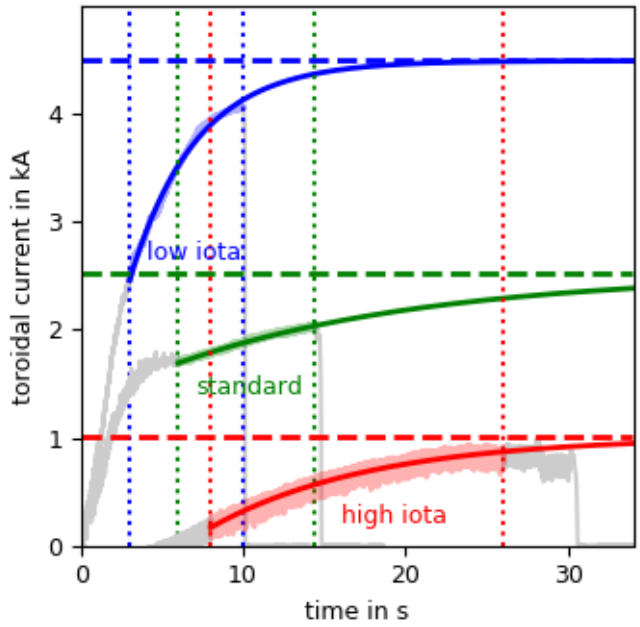

Figure 8. Dependence of the bootstrap current on the rotational transform: low-ɩ (blue), standard (green) and high-ɩ (red) magnetic configurations. Time traces and fit (solid lines), fitting window (dotted lines) and asymptotic value (dashed lines).

Reversal of the magnetic field direction (from low-ι to reversed-field low-ι magnetic configuration) leads to a reversal of the bootstrap current direction (figure 9). For this dependence, no experiment programs at identical densities were available. The programs shown were conducted at a heating power of 2 MW and line-integrated densities of 4.8 (normal), 4.4 and 5.2 (reversed) × 10^{19} m^{-2}. The linear dependency of the bootstrap current on the density found in section 3.2.3, however, allows for arithmetic averaging of the bootstrap current of the two reversed field programs. The difference in absolute value between the two field directions of 1.2 kA is well within the uncertainties of the measurements, but [Hammond 2019] reports on drift effects that could account for the difference.

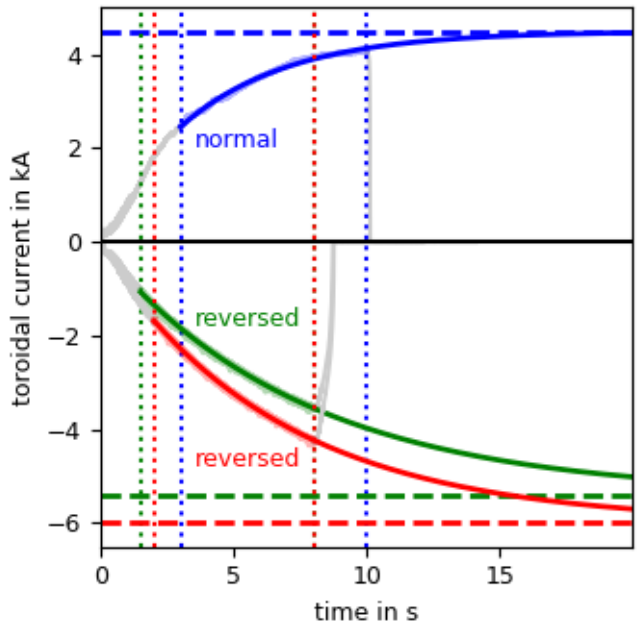

Figure 9. Effect of magnetic field reversal: normal (blue) and reversed (green and red) field direction. Time traces and fit (solid lines), fitting window (dotted lines) and asymptotic value (dashed lines).

3.2.2 Power dependence

In figure 10, bootstrap currents (experimental data [Neuner 2019] and data derived from NTSS simulations) are shown as a function of the heating power, with the line-integrated density as a colour-code. To guide the eye, lines were added to show the power dependencies within density intervals of 1 × 10^{19} m^{-2} width. For this, a linear regression was performed within each subgroup that included at least three data points, the reasoning for this being that the data does not support any higher orders. Where only two data points fall within a subgroup, these are connected by a straight line. This is also the case for the simulation data points, which are connected by a dashed line.

In the standard magnetic configuration, an increase in the heating power is associated with an increase in the bootstrap current for line-integrated densities below 10 × 10^{19} m^{-2}. The maximum gradient of 5.2 kA / MW is reached at a line-integrated density of 6 × 10^{19} m^{-2}. At line-integrated densities above 10 × 10^{19} m^{-2}, the bootstrap current stays almost constant during a variation of the heating power, the gradients remain positive but their absolute values are lower than the uncertainties in the measurements (figure 10a).

In all other magnetic configurations, an increase in the heating power is associated with an increase in the bootstrap current where data is available (figure 10b - e).

Comparing the measured dependence on power to a value obtained from two NTSS simulations, in the standard magnetic configuration at a line-integrated density of 5×10^{19} m^{-2}, the NTSS value of (3.7 ± 0.9) kA / MW is slightly lower than the experimental value of (4.4 ± 0.4) kA / MW (figure 10a). In the high-mirror magnetic configuration at a line-integrated density of 8×10^{19} m^{-2}, the NTSS value of (0.22 ± 0.42) kA / MW is lower than the experimental value of (1.03 ± 1.41) kA / MW (figure 10b). Both differences are, however, within the uncertainties.

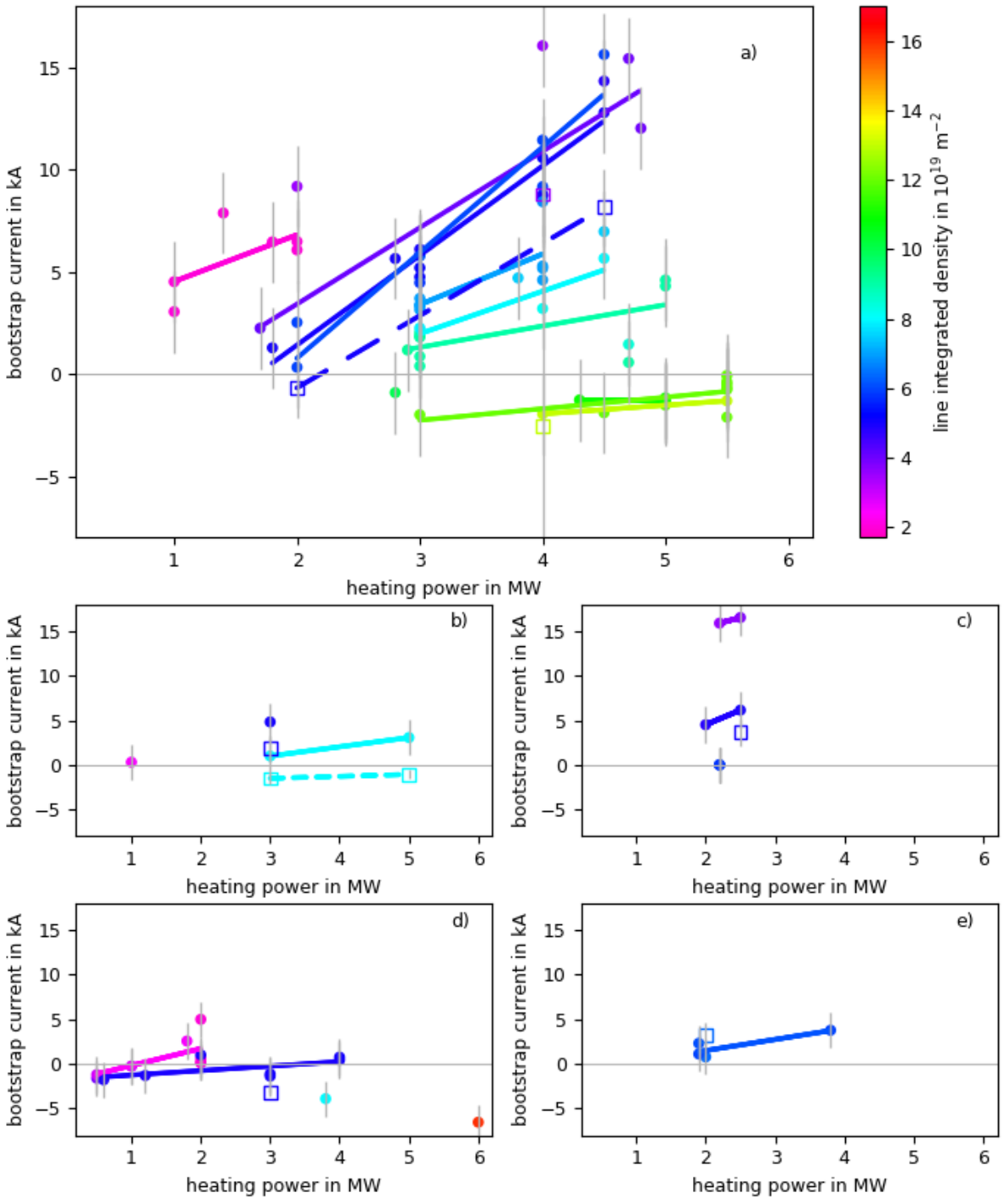

Figure 10. Dependence of the bootstrap current on the heating power (filled circles: experimental data, open squares: data derived from NTSS simulations, explanation of solid and dashed lines see text). a) Standard magnetic configuration (the colourbar is valid for all subplots). b) High-mirror magnetic configuration. c) Low-ι magnetic configuration. d) High-ι magnetic configuration. e) Intermediate-ι magnetic configuration.

3.2.3 Density dependence

Figure 11 depicts the same data as figure 10, only the power and density scales were switched. The bootstrap currents are shown as a function of the line-integrated density, with the heating power as a colour-code. To guide the eye, lines were added to show the density dependencies within power intervals of 0.5 MW width. For this, a linear regression was performed within each subgroup that included at least three data points, the reasoning for this being that the data does not support any higher orders. Where only two data points fall within a subgroup, these were connected by a straight line. This is also the case for the simulation data points, which were connected by a dashed line. No lines were added to subplot e) because its density variation is too small to draw any conclusions.

An increase in the density is associated with a decrease in the bootstrap current in the standard, the high-mirror and the high- and low-ι configurations (figure 11a - d). For intermediate-ι, no density dependence data is available since all measurements in this magnetic configuration were obtained at nearly the same density. The observed density dependence has only a small variation with the heating power. In the low-ι magnetic configuration, the gradient is pronouncedly steeper than in the other magnetic configurations (figure 11c).

Comparing the measured dependence on density to a value obtained from two NTSS simulations, in the standard magnetic configuration at a heating power of 4 MW, the NTSS value of (-1.2 ± 0.8) kA / $(10^{19}$ m$^{-2})$ is less steep than the experimental value of $(-1.8$ kA $\pm 0.1)$ / $(10^{19}$ m$^{-2})$ (figure 11a). In the high-mirror magnetic configuration at a heating power of 3 MW, the NTSS value of (-1.1 ± 0.5) kA / $(10^{19}$ m$^{-2})$ is slightly less steep than the experimental value of (-1.3 ± 0.9) kA / $(10^{19}$ m$^{-2})$ (figure 11b). Both differences are, however, within the uncertainties.

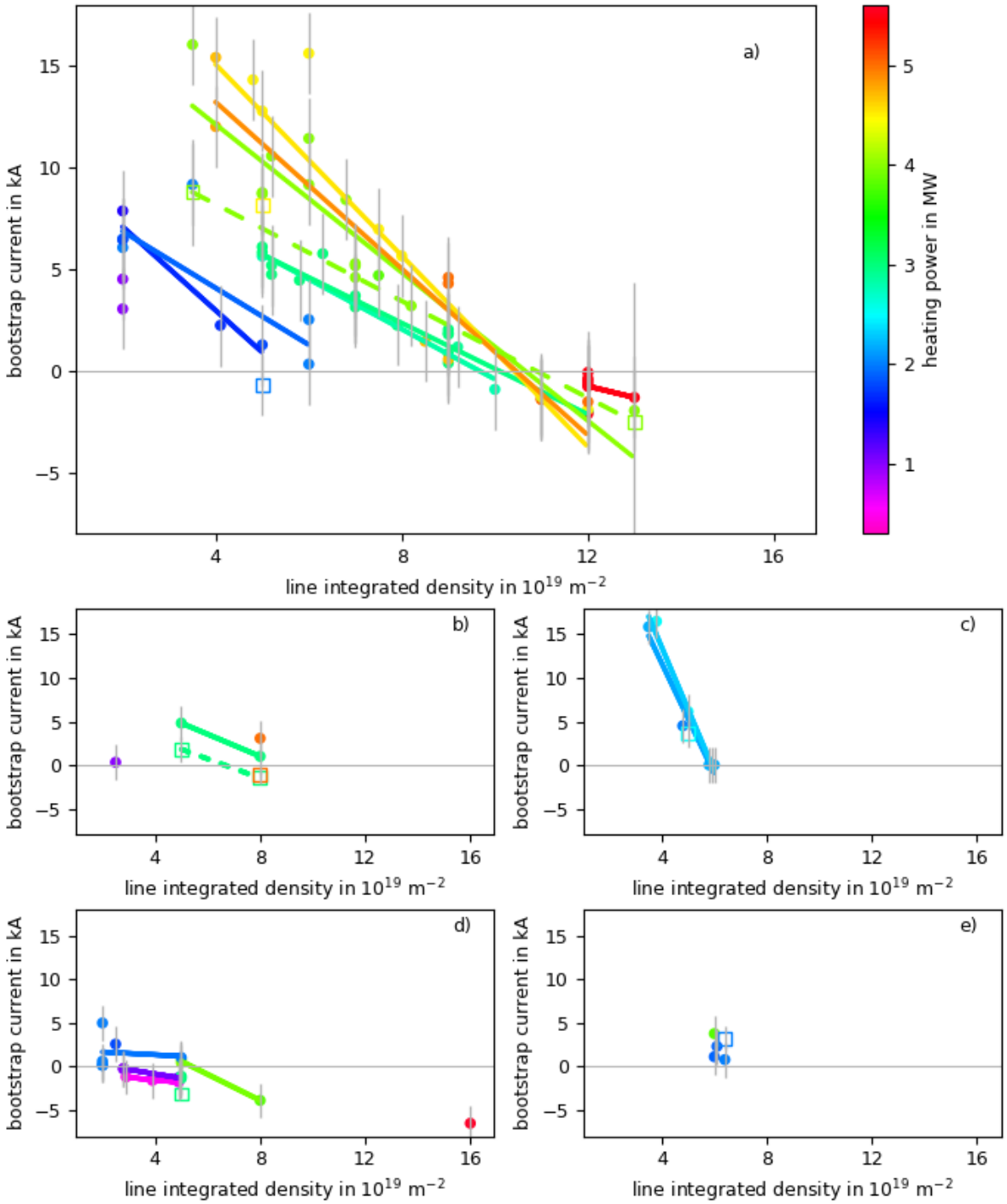

Figure 11. Dependence of the bootstrap current on the line-integrated density (filled circles: experimental data, open squares: data derived from NTSS simulations, explanation of solid and dashed lines see text). a) Standard magnetic configuration (the colourbar is valid for all subplots). b) High-mirror magnetic configuration. c) Low-ɩ magnetic configuration. d) High-ɩ magnetic configuration. e) Intermediate-ɩ magnetic configuration.

3.2.4 Dependence on temperature and density profiles and impurity content

The bootstrap current is affected by the detailed shape of the temperature and density profiles. To separate this effect from other influences, data at identical magnetic configurations, heating power

and line integrated density, but with differing shapes of the temperature and density profiles were compared. These were found early in the intervals of constant line-integrated density and heating power, where the temperature and density profiles are still evolving.

For the identical heating powers and line-integrated densities, neoclassical calculations with the NTSS code were performed for the differing, experimentally observed, temperature and density profiles. The effect of the latter on the bootstrap current was found to be at maximum 2 kA.

The effect of varying impurity contents was also studied in neoclassical calculations with the NTSS code. For two experimental programs in the high-mirror magnetic configuration (using the actually measured temperature and density profiles) even a variation of the effective charge state Z_{eff} of the plasma between 1 and 1.5, easily encompassing the measured values of 1.1 in these discharges, changed the bootstrap current by less than 0.7 kA.

Although these are only exemplary verifications, both the effect of the profile shape and of the impurity content on the bootstrap current were smaller than the effects of the magnetic configuration, the heating power and the plasma density (taking into account their total variation in the measurements). This was taken as a justification for the approach taken in this work to not distinguish between programs with differing profile shapes and impurity contents when looking for effects on the bootstrap current.

4. Discussion: Optimisation of W7-X

4.1 Neoclassical view on the dependencies

The comparisons between experimental results and the results of neoclassical calculations given in sections 3.1, 3.2.2 and 3.2.3 showed agreement, confirming the applicability of the neoclassical theory in the observed parameter range and the validity of the assumption that the observed currents flow mainly inside the separatrix.

To substantiate these specific comparisons, a more generalised view on the dependencies of the bootstrap current on the parameters is given, using an intermediate result of neoclassical theory [Beidler 2011], the monoenergetic transport coefficient D_{31}^{*} (calculated using the DKES code [van Rij 1989]) as a function of the collisionality v* (figure 12).

When increasing the mirror term from the standard to the high mirror configuration the positive values of the monoenergetic transport coefficient become less and less pronounced, while the number of negative values increases. This will decrease the originally positive bootstrap current and can make it zero or negative.

Increasing the rotational transform from the low-ι via the standard to the high-ι magnetic configuration, the same applies.

Increasing the heating power increases the temperature. Since collisionality is proportional to n/T^2 where *n* is the density and *T* is the temperature, this decreases the collisionality. A shift of the distribution function of collisionalities to the left in figure 12 leads to more and more pronounced

positive values and less negative values, generally increasing bootstrap currents. With increasing density, the rise in temperature associated with an increase in heating power is reduced.

Increasing the density at constant heating power decreases the temperature, so that both the change in density and in temperature increase the collisionality. A shift of the distribution function of collisionalities to the right in figure 12 leads to less and less pronounced positive values and more negative values, generally decreasing originally positive bootstrap currents or even making them zero or negative.

These considerations are of course greatly simplified, the effect of the radial electric field, for example, was omitted.

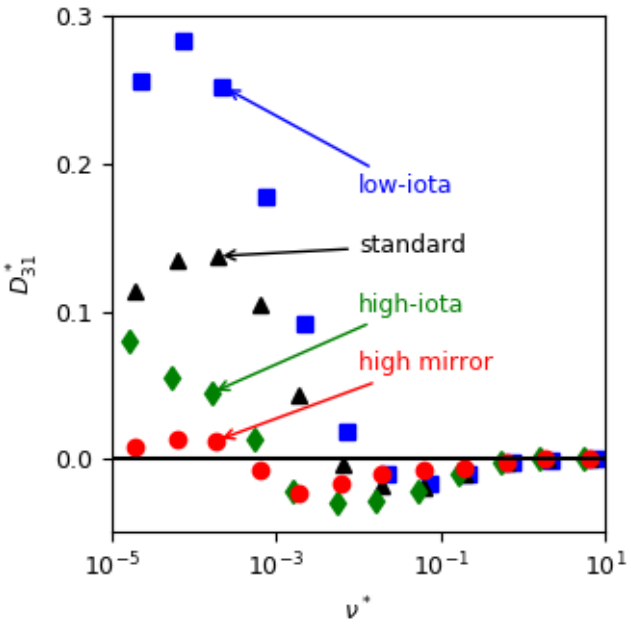

Figure 12. Monoenergetic transport coefficients as a function of collisionality for several magnetic configurations of W7-X at half-radius.

4.2 Effect of the measured currents on the W7-X performance

[Gao 2019] reports a strike line shift of 9 mm / kA in W7-X. Even with the largest current reported in this work, 17 kA, this would amount to a total shift of no more than 15 cm, a value easily compatible with the width of the divertor targets if the strike line can be placed in an appropriate region of the targets by a suitable choice of the magnetic field configuration. The pumping efficiency, however, could be compromised if the strike line is too far from the pumping gap.

The bootstrap current of W7-X has been reported to affect various parameters on the target surface (strike line position [Gao 2019, Killer 2019 PPCF], heat flux, flow, temperature, density) and in the scrape off layer (flows, separatrix position, temperature, density) [Killer 2019 PPCF, Killer 2019 NF, Drews 2019, Barbui 2019]. As an explanation, a change of the rotational transform, affecting the connection lengths, was inferred.

4.3 Extrapolation to future W7-X operation

Currently, a new, water-cooled, steady-state capable divertor is being installed in W7-X. This will facilitate longer experimental programs. At the same time, machine safety becomes a crucial aspect of day-to-day work. This is because an overloading of the former divertor would have led to carbon blooming, a loss of plasma energy by radiation, and consequentially an increase of the stray radiation of the ECRH, thereby triggering the safety interlock system and ending the program. Overloading the new divertor, in contrast, will immediately damage the divertor by breaking the bonding between the copper layer and the CuCrZr layer. Prediction and real time monitoring of the bootstrap current, the strike line position and the heat load on the divertor will therefore become mandatory.

The neoclassical calculation of the bootstrap current seems to be a useful tool for its prediction, given enough information on the plasma parameters. Real-time prediction using fast profile evaluation to control the strike line position has also been proposed [Dinklage 2020].

The high-mirror and the high-ι magnetic configurations have proven to yield small bootstrap currents. But also in the standard magnetic configuration, the small dependence of the bootstrap currents on the heating power at the higher densities as measured so far allows to be hopeful for the future. The bootstrap current may still be in the acceptable range when extrapolating to even larger heating powers in this density range and above, which is considered the reactor relevant region.

On the other hand, the combination of low density, large heating power and an unfavourable magnetic configuration like low-ι or standard will probably lead to problematically large bootstrap currents.

Another direction W7-X will take, however, is towards steeper profiles. Reduction of the turbulence will increase ion temperatures and likely bootstrap currents. During OP1.2b, the confinement was improved when the pressure profile was temporarily steepened by injection of hydrogen pellets [Klinger 2019, Bozhenkov 2020]. With the planned steady-state pellet injector the profile effect on the bootstrap current could then become as important as the effects of magnetic configuration, heating power and density discussed in this work and hence must be investigated.

4.4 Mitigation techniques

Where the bootstrap current is larger than the acceptable limit, it might still be small enough that its effect can be mitigated.

ECCD has been employed to lower the total toroidal current at W7-X [Stange 2017], cancelling its effect on the edge plasma. However, strong shear might compromise the stability [Geiger2010].

When the bootstrap current is so large that the sweep of the strike line during the decay of the shielding current exceeds the width of the target, the experimental program could be designed in such a way that the final configuration yields no problem, limiting the potentially dangerous scenarios to the beginning or an intermediate phase. Such phases could then be run at low power or they could be accelerated to limit the total energy deployed onto critical components [Sinha 2019]. Possible means to achieve this would be current drive, large bootstrap current phases, or current ramps in the magnetic field coils. When the current in the planar coils of W7-X can be swept fast enough, the effect of the bootstrap current on the edge ι might even be cancelled over the whole program. Still one more

possibility is given by specific components temporarily shielding sensitive parts [Lore 2014, Lumsdaine 2016].

5. Summary and Conclusions

A method for inferring the bootstrap current has been introduced for experimental programs in which the plasma parameters can be kept constant over an interval in the order of one decay time of the shielding current. Bootstrap currents were measured over a wide range of magnetic field and plasma parameters. The presented data allows to separate the effects of the variation of the magnetic configuration, the heating power and the plasma density.

The experimental results agree with neoclassical calculations both in absolute value and in the dependencies on the parameters of the magnetic field and the plasma within their respective uncertainties.

The wide parameter space covered allows to predict bootstrap currents for many future experiments either directly from the measurements or via benchmarked neoclassical calculations.

The neoclassical optimisation of W7-X for sufficiently small bootstrap currents was confirmed in the observed parameter space, promising wide operational capabilities both for W7-X as well as for future machines in the HELIAS line following a similar optimisation.

Acknowledgement

This work has been carried out within the framework of the EUROfusion Consortium and has received funding from the Euratom research and training programme 2014-2018 and 2019-2020 under grant agreement number 633053. The views and opinions expressed herein do not necessarily reflect those of the European Commission.

References

Nührenberg J., Zille R. 1986 *Phys. Lett.* A **114** 129

Klinger T. *et al* 2013 *Fus. Eng. Des.* **88** 461

Klinger T. *et al* 2019 *Nuclear Fusion* **59** 112004

Sereda S. *et al* 2020 *Nucl. Fusion* **60** 086007

Hogan J.T. 1981 *Nucl. Fusion* **21** 365

Bickerton R.J. *et al* 1971 *Nature Physical Science* **229** 110

Galeev A.A. 1971 *Sov. Phys. JETP* **32** 752

Catto P., Helander P. 2020 *J. Plasma Phys.* **86** 905860105

Maassberg H., Lotz W., Nührenberg J. 1993 *Physics of Fluids* B: *Plasma Physics* **5** 3728

Maaßberg H., Beidler C.D., Turkin Y. 2009 *Phys. Plasmas* **16**, 072504

Geiger J. *et al* 2010 *Contrib. Plasma Phys.* **50** No. 8 770

Lore J.D. *et al* 2014 *IEEE Trans. Plasma Sci.* **42** No. 3 539

Lumsdaine A. *et al* 2016 *IEEE Transactions on Plasma Science* **44** No. 9 1738

Boozer A.H., Gardner H. 1989 Bootstrap current in stellarators *Proc. of the 7th Workshop on Stellarators (Oak Ridge, USA, 10 - 14 April 1989) IAEA-TECDOC-558* 607

Beidler C. *et al* 1990 *Fusion Technology* **17** 148

Grieger G. *et al* 1992 *Phys. Fluids* B **4** 2081

Grieger G. *et al* 1992 *Fusion Technol.* **21** 1767

Helander P., Nührenberg J. 2009 *Plasma Phys. Control. Fusion* **51** 055004

Helander P., Geiger J., Maaßberg H. 2011 *Phys. Plasmas* **18** 092505

Zarnstorff M.C., Prager S.C. 1984 *Phys. Rev. Letters* **53** 454

Treffert J.D., Shohet J.L., Berk H.L. 1984 *Phys. Rev. Lett.* **53** 2409

Besshou S. *et al* 1984 *Plasma Phys. Control. Fusion* **26** 565

Gutarev Yu.V. *et al* 1987 *Pis'ma Zh. Eksp. Teor. Fiz.* **46** No.2 60

Gasparino U. *et al* 1988 *Plasma Phys. Control. Fusion* **30** 283

Okamoto M., Nakajima N. 1990 Bootstrap Currents in Stellarators and Tokamaks, NIFS-53

Huang B. *et al* 2017 *Plasma and Fusion Research* **12** 1203004

Murakami M. *et al* 1991 *Phys. Rev. Lett.* **66** 707

Erckmann V. *et al* 1992 *Plasma Phys. Control. Fusion* **34** 1917

Isobe M. *et al* 2002 *Plasma Phys. Control. Fusion* **44** A189

Nagasaki K. *et al* 2006 Control of Non-Inductive Current in Heliotron J, *Proceedings of the 21st IAEA Conference ("Fusion Energy 2006") (Chengdu, China, 16* - 21 *October 2006) IAEA-CN-149*

Schmitt J.C. *et al* 2007 Measurement of the Pfirsch-Schlüter and Bootstrap Currents in HSX, *Proceedings of ITC/ISHW2007 (Ceratopia Toki, Gifu, Japan, 15-19 October 2007)*

Pashnev V.K., Sorokovoy E.L. 2008 *Probl. At. Sci. Technol.* No. 6 31

Velasco J.L. *et al* 2011 *Plasma Phys. Control. Fusion* **53** 115014

Camacho K., Martinell J.J. 2017 *Radiation Effects and Defects in Solids Incorporating Plasma Science and Plasma Technology* **172** Issue 1-2 108

Klinger T. *et al* 2017 *Plasma Phys. Control. Fusion* **59** 014018

Wolf R. *et al* 2017 *Nucl. Fusion* **57** 102020

Sunn Pedersen T. *et al* 2017 *Phys. Plasmas* **24** 055503

Dinklage A. *et al* 2018 *Nature Physics* **14** 855

Andreeva T. *et al* 2019 *Fusion Eng. Des.* **146** 299

Turkin Y. *et al* 2006 *Fusion Sci. Technol.* **50** 387

Turkin Y. *et al* 2011 *Physics of Plasmas* **18** 022505

Endler M. *et al* 2015 *Fusion Eng. Des.* **100** 468

Rahbarnia K. *et al* 2016 *43rd EPS Conference on Pl. Phys. (Leuven, Belgium, 4 - 8 July 2016)* P4.011

Werner A. 2006 *Rev. Sci. Instrum.* **77** 10E307

Rahbarnia K. *et al* 2018 *Nucl. Fusion* **58** 096010

Neuner U. *et al* 2017 *Fusion Eng. Des.* **123** 923

Hammond K.C. *et al* 2019 *Plasma Phys. Control. Fusion* **61** 125001

Rack M. *et al* 2012 *Nucl. Fusion* **52** 074012

Dhard C.P. *et al* 2020 *Phys. Scr.* **2020** 014033

Marushchenko N.B., Turkin Y., Maassberg H. 2014 *Computer Physics Communications* **185** 165

Kapper G. *et al* 2016 *Phys. Plasmas* **23** 112511

Andreeva T. *et al* 2002 *Problems of Atomic Science and Technology, Series: Plasma Physics* **4** 45

Geiger J. *et al* 2015 *Plasma Phys. Control. Fusion* **57** 014004

Krychowiak M. *et al* 2016 *Rev. Sci. Instrum.* **87** 11D304

Svensson J., Werner A. 2007 Large Scale Bayesian Data Analysis for Nuclear Fusion Experiments, *Proceedings IEEE Workshop on Intelligent Signal Processing WISP 2007 (Alcala de Henares, Madrid, Spain, 2 - 5 October 2007)*

Pasch E. *et al* 2016 *Rev. Sci. Instrum.* **87** 11E729

Knauer J. *et al* 2016 *43rd EPS Conference on Plasma Physics (Leuven, Belgium, 4 - 8 July 2016)* P4.017

Pablant N.A. *et al* 2016 *43rd EPS Conference on Plasma Physics (Leuven, Belgium, 4 - 8 July 2016)* P4.013

Langenberg A. et al 2019 *Rev. Sci. Instrum.* **90** 063505

Pavone A. *et al* 2019 *JINST* **14** C10003

Pavone A. *et al* 2020 *JINST* **15** e02002

Hirshman S., van Rij W., Merkel P. 1986 *Comput. Phys. Comm.* **43** 143

Grahl M. *et al* 2017 Web Services for 3D MHD Equilibrium Data at Wendelstein 7-X, *Proc. 27th IEEE Symposium on Fusion Engineering (Shanghai, China, 4 - 8 June 2017)*

Chilenski M.A. *et al* 2015 *Nucl. Fusion* **55** 023012

Yokoyama, M. *et al* 2007 *Nuclear Fusion* **47** 1213

Pablant, N.A. *et al* 2018 *Phys. Plasmas* **25** 022508

Neuner U. *et al* 2019 *Proceedings of the 46th EPS conference on Plasma Physics (Milan, Italy, 8- 12 July 2019)* P2.1065

Beidler C.D. 2011 *Nucl. Fusion* **51** 076001

van Rij W.I., Hirshman S.P. 1989 *Phys. Fluids* B **1** 563

Gao Y. *et al* 2019 *Nuclear Fusion* **59** 106015

Killer C. *et al* 2019 *Plasma Phys. Control. Fusion* **61** 125014

Killer C. *et al* 2019 *Nucl. Fusion* **59** 086013

Drews P. *et al* 2019 *Nuclear Materials and Energy* **19** 179

Barbui T. *et al* 2019 *JINST* **14** C07014

Dinklage A. *et al* 2020 Theory-based models for the control of W7-X divertor plasmas*, 28th IAEA Fusion Energy Conference (FEC2020) (Nice, France, 10 - 15 May 2021)*

Bozhenkov S.A. *et al* 2020 *Nucl. Fusion* **60** 066011

Stange T. *et al* 2017 Advanced electron cyclotron heating and current drive experiments on the stellarator Wendelstein 7-X, *EPJ Web Conf.* ***157*** *22 Topical Conference on Radio-Frequency Power in Plasmas (Aix-en-Provence, France, 30 May - 2 June, 2017)* 02008

Sinha P. *et al* 2019 *Nucl. Fusion* **59** 126012